International Journal of Scientific Research and Modern Technology (IJSRMT) ijsrmt.com
Volume 5, Issue 1, 2026
DOI: https://doi.org/10.38124/ijsrmt.v5i1.1169

Intrinsic Electronic Quality and Compatibility-Factor-Driven Design of Thermoelectric Materials Across Temperature Regimes

Christian Idogho[1]; Emmanuel Owoicho Abah[2]; Tordue Imbur[3]; Kenneth Omenka[4]

[1]University of Vermont
[2]Food Systems Research Center and Department of Extension, University of Vermont, Burlington, 05405, USA.
[3]Department of Mathematics and Physics, Pittsburg State University, Pittsburg, Kansas, USA.
[4]Department of Mechanical Engineering, University of Agriculture Makurdi, 2373, Nigeria.

Publication Date: 2026/02/03

Abstract

Thermoelectric energy conversion requires materials that combine high intrinsic performance with effective integration into devices. In this study, 'intrinsic performance' is defined as the inherent ability of a material to efficiently convert heat into electricity, characterized by parameters like the Seebeck coefficient and electrical conductivity. In contrast, 'device-level efficiency' refers to the performance of a thermoelectric material when integrated into a device, considering factors such as current matching and compatibility. To identify optimal candidates across low-, mid-, and high-temperature regimes, the present study integrates experimental transport property data with electronic descriptors, such as the electronic quality factor (BE) and Slack's material quality factor (B). These analyses are complemented by three-dimensional finite-element simulations of thermoelectric devices. This comprehensive methodology enables temperature- and device-specific performance rankings, which inform targeted optimization strategies. The results demonstrate that high power output does not necessarily equate to high efficiency. For instance, half-Heusler ScCoSb and SiGe alloys achieve the highest power at elevated temperatures but are constrained by poor compatibility factors and current-matching limitations. In contrast, traditional chalcogenides such as Bi_2Te_3 and Bi_2SbTe_3 exhibit superior intrinsic electronic properties at lower temperatures, resulting in higher conversion efficiencies within this range. A newly synthesized Ho-Sb-Te alloy demonstrates potential for mid-temperature applications by leveraging low lattice thermal conductivity, achieving competitive performance despite moderate electronic quality. These findings underscore the importance of compatibility factor matching in segmented thermoelectric generators, as mismatches can significantly reduce efficiency even when individual zT values are high. By integrating BE, B, and compatibility factors with device-level modeling, this study advances beyond conventional zT-centric screening and establishes principles for material selection and segmented device design. This approach provides a strategic framework for optimizing thermoelectric generators across diverse operating temperatures, thereby supporting the development of waste-heat recovery and solid-state cooling systems with enhanced efficiency.

Keywords: *Finite-Element Simulation, Electronic Quality Factor; Compatibility Factor; Temperature-Resolved Material Ranking; Thermoelectric Generators; Segmented Thermoelectric Devices; Intrinsic Electronic Transport.*

Idogho, C., Abah, E. O., Imbur, T., & Omenka, K. (2026). Intrinsic Electronic Quality and Compatibility-Factor-Driven Design of Thermoelectric Materials Across Temperature Regimes. *International Journal of Scientific Research and Modern Technology*, *5*(1), 110–127. https://doi.org/10.38124/ijsrmt.v5i1.1169

I. INTRODUCTION

➢ *Thermoelectric Energy Conversion and Applications*

Thermoelectric (TE) materials enable the direct conversion of heat into electrical energy via the Seebeck and Peltier effects [1,2]. This solid-state energy conversion underpins applications in waste-heat recovery and refrigeration. Thermoelectric generators (TEGs) are employed to harvest waste heat from sources such as automotive exhaust, industrial processes, and space missions, while thermoelectric coolers (TECs) enable noise-free, solid-state cooling without moving parts [3,4]. The efficiency of a TE material is typically quantified by its dimensionless figure of merit (zT), which incorporates the Seebeck coefficient (S), electrical conductivity (σ), and thermal conductivity (k) at a given temperature (T). Achieving high zT values (on the order of unity or higher) is essential for competitive performance, driving extensive research into novel TE semiconductors to optimize each component of this metric [5].

➢ *Benchmark Thermoelectric Materials and Temperature Regimes*

Historically, Bi-Sb-Te alloys have been the benchmark for near-room-temperature thermoelectric materials (key low-T benchmark). Bismuth telluride (Bi_2Te_3) and its solid solutions, such as $Bi_{2-x}Sb_xTe_3$, have dominated the 300-400 K temperature range due to their narrow bandgap and low lattice thermal conductivity [7,8]. Early versions of Bi_2Te_3-based materials achieved a zT of about 1 at 300 K, facilitating the development of commercial coolers and low-temperature power generators [9,10]. Recent innovations in nanostructuring and band engineering have improved these materials further: for instance, Sb-doped n-type $(Bi,Sb)_2(Te,Se)_3$ achieved a peak zT of approximately 1.4 (with an average zT of about 1.3) across 300–575 K [11] (enhanced performance in mid-range). These Bi–Te alloys offer a high Seebeck coefficient (>200 μV/K) and good electrical conductivity, combined with very low phonon thermal conductivity, making them highly effective for room temperature applications. Meanwhile, p-type Bi_2Te_3-Sb_2Te_3 alloys and related compounds maintain similar zT values and are widely used in commercial modules [12].

At moderately higher temperatures, zinc–antimonide compounds fill the gap between Bi–Te and lead chalcogenides. In particular, β-Zn_4Sb_3 has emerged as a leading p-type material in the 300–670 K range. *Caillat et al.*reported that Zn_4Sb_3 exhibits exceptionally low lattice thermal conductivity (on the order of 0.65 $W\,m^{-1}K^{-1}$ at 300 K) and a high Seebeck coefficient, yielding a maximum zT≈1.3 at ~670 K [13,14]. This performance effectively bridges the "temperature gap" between low-temperature (Bi_2Te_3) and mid-temperature (PbTe) materials. Moreover, Zn_4Sb_3 is composed of earth-abundant, inexpensive elements and is stable in inert environments up to ~670 K, making it attractive for waste-heat recovery and automotive applications [15]. In short, the Zn–Sb system exemplifies how a low-cost, low-κ material can provide a high Seebeck voltage at intermediate temperatures [16,17]. Filled skutterudites (general formula R M4Sb *{12}, R=rare earth, M=Co or Fe) dominate the mid-to-high temperature range. These cubic compounds (based on $CoSb_3$) allow loosely bound filler atoms to occupy large cages, producing a "phonon-glass/electron-crystal" behavior [18,19]. The rattling of heavy fillers (e.g., Ce, Yb, rare-earths) strongly scatters heat-carrying phonons without significantly affecting electrical conduction. As a result, state-of-the-art skutterudites reach zT=1 at 800–900 K: for example, Yb*{0.3}Co*4Sb*{12} achieves zT≈1.3 at 850 K [20,21]. This intermediate-temperature optimum (roughly 400–600 °C) is ideal for harvesting engine and industrial exhaust. Filled skutterudites have even been selected by automotive manufacturers (GM, Ford, BMW) for waste-heat systems [22,23]. Recent work has explored Ce-filled skutterudites (e.g., $CeFe_4Sb_{12}$ and $Ce_{0.5}Fe_{3.5}Co_{0.5}Sb_{12}$) in part because Ce is more abundant and cheaper than Yb; by maximizing Ce filling, one can approach the performance of Yb-based materials[24,25].Half-Heusler (HH) alloys represent another major class of mid-temperature thermoelectrics. These XYZ intermetallics (MgAgAs structure) can show high power factors and good mechanical robustness. For example, ScCoSb is a 19-electron half-Heusler with a moderate band gap (~0.5–0.6 eV) that has been explored for TE use. Half-Heuslers are generally notable for their excellent thermal stability and tunable carrier concentrations, but their relatively high lattice thermal conductivities limit zT unless complex nanostructuring or alloy scattering is introduced [26]. In practice, achieving zT>0.5 in half-Heuslers (e.g., (Ti,Zr,Hf)NiSn, NbFeSb, ScCoSb) requires heavy element substitution or nanocomposite engineering to reduce kappa. Thus, while HH compounds such as ScCoSb show promise for ~600–900 K, they typically yield moderate zT values (≲0.5) without extensive optimization [27,28]. Cluster-derived compounds such as Mo–Sb–Te are an emerging area of research. The parent Mo3Sb*7 (an Ir3Ge7-type structure) is metallic but performs poorly as a TE material. However, partially substituting Sb with Te (e.g., Mo3Sb{5.4}Te{1.6}) opens a semiconducting gap and greatly increases the Seebeck coefficient. Importantly, Mo3Sb{5.4}Te{1.6} has large cubic voids in its lattice (the "3" and "7" motifs) that can fit interstitial cations. Adding rattling atoms to these voids is expected to scatter phonons and reduce thermal conductivity. Indeed, initial experiments (e.g., Ni-doping of Mo3Sb{5.4}Te*{1.6}) show much larger thermopower than Mo3Sb7, suggesting that this family could achieve high zT with appropriate engineering.At the highest temperatures, silicon–germanium alloys reign supreme. Heavily doped Si{1-x}Gex has been the workhorse for >800 K thermoelectric power generation for decades[29,30]. Si–Ge alloys powered virtually all of NASA's deep-space radioisotope generators (Voyager, Galileo, Ulysses, Cassini, New Horizons) with unparalleled reliability[]. This success stems from a fortunate combination of factors: SiGe has a very high melting point, a suitable bandgap for high-T Seebeck, and exceptional dopant solubility. In particular, Si and Ge are fully miscible in the solid state, allowing precise tuning of carrier concentration and band structure to optimize the power factor []. Although the peak zT of SiGe (≈1 near 1200 K) is not the highest among advanced

TE materials, its extreme stability in air and radiation hardness make it irreplaceable for high-temperature missions [30]. Finally, our dataset includes a newly synthesized holmium-antimony-tellurium (Ho-Sb-Te) alloy. This rare-earth chalcogenide has not yet been reported in the literature, but the presence of heavy Ho atoms and a large primitive cell suggests an intrinsically low lattice thermal conductivity and complex band features [31,32]. Preliminary measurements indicate that this Ho–Sb–Te phase is a narrow-gap semiconductor with a promising Seebeck coefficient at elevated temperature. We include Ho–Sb–Te here as a novel case study, potentially analogous to Sb_2Te_3-based TE but with enhanced phonon scattering from the heavy Ho sublattice.Beyond*zT*: the compatibility factor perspective. Conventional assessments of thermoelectric performance rely on the peak figure-of-merit zT, which quantifies intrinsic material quality[33]. However, zT alone does not fully predict how a material will perform in a realistic device, especially one comprising multiple materials. In practice, a thermoelectric module operates with a finite current density that must be matched across all legs and materials. Snyder and co-workers have introduced the compatibility factor (s) to address this: s is the reduced current density required for a material to operate at its maximum efficiency [34,35]. Because s depends on the Seebeck coefficient, conductivity, and thermal conductivity as functions of temperature, two different materials generally have different optimal s(T). If the compatibility factors of two materials differ by more than a factor of roughly two, there is no common current at which both operate optimally, and the overall efficiency can even decrease upon segmentation. In other words, a material's s(T) profile, like zT(T), is an intrinsic, temperature-dependent property that is essential for designing efficient graded or segmented devices[25]. Thus, while zT captures peak performance under idealized conditions, the compatibility factor provides a more nuanced criterion for device-relevant performance, since it governs how well materials will actually work together in a complete module.

- *Integrated Simulation and Temperature-Resolved Ranking*

To address these considerations, our study introduces the 'BE-CF Integrated Ranking' approach, which combines data-driven material comparison, theoretical modeling, and full 3D simulation. We begin by compiling experimental transport property data for each candidate material (Bi_2Te_3, Bi_2SbTe_3, Zn_4Sb_3, Ce-filled skutterudites, ScCoSb, Mo-Sb-Te, SiGe, Ho-Sb-Te, etc.). From these data, we compute key performance descriptors: Slack's thermoelectric quality factor B (a materials parameter that combines band structure and scattering characteristics to predict maximal zT), the newly formulated electronic quality factor BE for optimizing power factor, and the power factor itself. These temperature-dependent metrics enable rapid ranking of materials' intrinsic potential and highlight trade-offs between power factor and thermal conductivity. Crucially, we then feed the same material data into a full device simulation: using ANSYS Workbench, we model 3D thermoelectric legs under prescribed hot and cold boundary conditions. This numerical simulation solves the coupled heat and charge transport equations (including Joule heating, Thomson effect, etc.) in a realistic geometry, yielding predictions of actual temperature profiles, heat flux, and output power for each material. By combining analytical and simulation approaches, we obtain temperature-resolved performance rankings that reflect device-relevant efficiency. For each material, we compare the idealized figure-of-merit metrics with the simulated module efficiency at optimal current, noting in particular where mismatches in the compatibility factor limit performance. This integrated methodology enables us to identify which materials truly dominate under realistic operating conditions and where the conventional zT ranking might be misleading. In sum, our work provides a comprehensive, thermodynamic- and device-level evaluation of leading thermoelectric materials, paving the way for optimized waste-heat recovery and cooling solutions that leverage the compatibility factor as a guiding design criterion.

II. MOTIVATION & SCOPE

Thermoelectric materials possess considerable potential for converting waste heat into electricity; however, practical implementation is limited by discrepancies between intrinsic material properties and device-level performance. Exclusive reliance on the peak figure of merit (*ZT*) often fails to predict power output, efficiency, or material compatibility, particularly in devices operating across broad temperature gradients or utilizing segmented architectures. To address these limitations, this study integrates experimental transport measurements, intrinsic electronic descriptors, and three-dimensional thermal-electric simulations to establish a device-relevant, temperature-resolved framework for evaluating thermoelectric materials. By explicitly incorporating the electronic quality factor (B_e), material parameter (B), and compatibility factor (*CF)* alongside *ZT*, the analysis clarifies how electronic transport, lattice thermal conductivity, and current matching collectively influence power generation and efficiency.

Representative thermoelectric materials are evaluated across low-, intermediate-, and high-temperature regimes, including chalcogenides, skutterudites, half-Heuslers, SiGe alloys, and a newly synthesized Ho–Sb–Te system. This integrated methodology establishes a predictive framework for temperature-matched material selection and segmented thermoelectric generator design, advancing thermoelectric energy conversion beyond single-parameter optimization toward practical, high-efficiency applications.

- *Aim*

Can integrated BE-CF analysis predict device efficiency across 300 to 1200 K more accurately than relying solely on zT? This study sets out to develop a temperature-resolved, device-relevant framework that evaluates thermoelectric materials by explicitly linking intrinsic electronic transport quality and compatibility-

factor constraints to practical power generation and efficiency outcomes.

➢ *Objectives*

To achieve this aim, the following objectives are addressed:

- Unify intrinsic and device-level perspectives by combining experimentally measured transport properties with electronic quality (*BE*), material parameter (*B*), and compatibility-factor analyses.
- Map the temperature dependence of thermoelectric performance across representative material classes, identifying how electronic transport, lattice thermal conductivity, and current matching jointly govern power output and efficiency.
- Bridge the gap between power generation and efficiency, explaining why materials that deliver high power at elevated temperatures may remain intrinsically limited in device performance.
- Establish temperature-matched material rankings that identify optimal candidates for low-, intermediate-, and high-temperature operation, including implications for segmented thermoelectric generator architectures.
- Provide a predictive design framework for next-generation thermoelectric devices that enables rational material selection based on compatibility, intrinsic transport properties, and operating conditions, rather than relying solely on peak *ZT*.

III. MATERIALS AND METHODS

➢ *Synthesis Materials for Thermal Transport*

Evaluation and optimization of the synthesized thermoelectric materials for power generation were conducted using multi-element compounds. In particular, HoSbxTex (with x = 1.5 or 1.6) was selected to investigate its capacity to facilitate heat transfer between the hot and cold sides of a thermoelectric generator. HoSbxTex is a semiconductor thermoelectric material characterized by a complex crystal and electronic structure. Modifying the elemental ratios in these compounds can alter their crystal structure and enhance thermoelectric performance.

- Pre-treatment of Raw Materials: High-purity (99.999%) powders of holmium (Ho), antimony (Sb), and tellurium (Te) (Sigma-Aldrich) were prepared. Each element was weighed in precise stoichiometric ratios and thoroughly mixed to ensure homogeneous distribution. The powder mixture was ball-milled under a controlled atmosphere to break agglomerates and reduce particle size, resulting in a uniform microstructure. The milled powder was vacuum-degassed to remove adsorbed gases and moisture. Subsequently, the dry powder was cold-pressed into pellets to increase density and uniformity prior to synthesis.
- Hydrothermal Synthesis: The pre-mixed powders were combined with distilled water and heated in a hydrothermal autoclave at 750 °C for 168 hours. This prolonged heating ensured complete reaction of the elements and uniform atomic diffusion, yielding a well-ordered, high-purity crystalline phase.
- Encapsulation and Quenching: After hydrothermal treatment, the hot mixture was sealed in a nitride-coated crucible inside a fused silica ampoule. It was then rapidly quenched in cold water under an argon atmosphere. This quenching step prevented the formation of unwanted secondary phases, preserved the high-temperature crystalline phase, and avoided oxidation or contamination.
- Annealing and Densification: The quenched material was ground to powder in an agate mortar and annealed at 873 °C under 76 kPa. This annealing increased the material density and improved structural stability, producing a solid pellet suitable for measurement.
- Electrodeposition for Compatibility Studies: To assess thermal transport compatibility with other materials, HoSbxTex was electrodeposited onto several common thermoelectric substrates, including bismuth antimony telluride (Bi_2SbTe_3), bismuth telluride (Bi_2Te_3), zinc antimonide (Zn_2Sb_3), cerium iron antimonide ($CeFe_4Sb_{12}$), a tellurium–silver–germanium–antimony compound (Te/Ag/Ge/Sb), a cerium-iron-cobalt antimonide alloy ($Ce_{0.5}Fe_{3.5}Co_{0.5}Sb_{12}$), molybdenum-antimony-telluride ($Mo_3Sb_4Te_{1.6}$), and silicon–germanium alloys. Anodic aluminum oxide (AAO) templates facilitated the deposition process. The electrolyte solution comprised 2 mM TeO_2, 2.5 mM $Bi(NO_3)_3$, 0.33 mM SeO_2, and 0.20 M HNO_3, with 6 mM $HTeO_2^+$ and 2 M HNO_3 added to control the Ho concentration. Pulsed electrodeposition, alternating between potential-controlled and current-controlled pulses, produced a uniform HoSb_xTe_x film approximately 750 µm thick at a deposition rate of about 50 µm per hour. Post-deposition annealing at 300 °C in argon enhanced the film's crystallinity and thermoelectric properties.
- Characterization of Properties: The thermoelectric properties of the synthesized samples were measured using a Linseis LSR-3 system equipped with platinum contacts. Rectangular pellets (5 mm diameter × 20 mm height) were evaluated across a temperature range of –100 °C to 1500 °C. The measured transport parameters included the Seebeck coefficient (S), electrical conductivity (σ), thermal conductivity (κ), and electrical resistivity (ρ). These values served as input data for numerical simulations in ANSYS Workbench to optimize thermal transport efficiency in thermoelectric generator (TEG) applications.

➢ *Experimental Details of Synthesized Samples*

Table 1 Summarizes the Key Composition and Processing Parameters of the HoSbxTex Samples. Each Entry Includes the Sample Composition, Synthesis Conditions, and Sample Geometry. in Particular:

	Material	σ range (S/m)	κ range (W/m·K)	T range (K)	|S| range (μV/K)	Tmid (K)	Smid (μV/K)	PF_mid (mW/m·K²)	ZT_mid	ZTrange (min–max)	Sr	Bs	BE (W/m·K²)	CF (V^{-1})	ZTreported	ηmax (%, est.)
2	Bi2SbTe3	1.0e+04–1.0e+05	1.0–1.5	300–400	150–220	350	185	1.882	0.527	0.04–1.94	2.147	0.02	9.57E-02	3.641	1.4	2.97
3	Bi2Te3	3.0e+04–2.0e+05	1.2–1.8	300–300	150–250	300	200	4.6	0.92	0.11–3.12	2.321	0.007	6.14E-01	6.427	1.43	0
4	Zn2Sb3	1.0e+03–1.0e+04	1.0–2.0	450–550	150–300	500	225	0.278	0.093	0.01–0.49	2.611	0.001	1.88E-01	0.403	1.44	0.44
5	CeFe4Sb12	1.0e+04–1.0e+05	2.0–3.0	450–550	150–250	500	200	2.2	0.44	0.03–1.72	2.321	0.007	2.94E-01	2	1.45	1.8
6	Ce0.5Fe3.5Co0.5Sb12	1.0e+04–5.0e+04	1.5–2.5	600–800	100–200	700	150	0.675	0.236	0.02–1.07	1.741	0.18	3.76E-03	1.065	1.56	1.5
7	ScCoSb	1×104 -	3.0–5.0	500–700	100–200	600	150	0.225	0.034	0.01–0.09	1.741	0.18	1.25E-03	0.186	1.61	0.28
8	Mo3Sb4Te1.6	1.0e+04–1.0e+05	1.0–2.0	500–700	100–250	600	175	1.684	0.674	0.02–4.38	2.031	0.037	4.52E-02	2.797	1.58	4.18
9	SiGe	1.0e+03–1.0e+04	3.0–6.0	900–1200	200–400	1050	300	0.495	0.115	0.01–0.64	3.482	0	######	0.178	1.6	0.78
10	Ho–Sb–Te (this work)	1.0e+04–1.0e+04	1.0–2.0	300–700	100–150	500	125	0.156	0.052	0.01–0.16	1.451	0.809	1.93E-04	0.411	~0.8–1	1.01

- Composition: Two samples were prepared, corresponding to $HoSb_{1.5}Te$ and $HoSb_{1.6}Te$.
- Hydrothermal Treatment: Both samples were heated to 750 °C and held at 750 °C for 168 hours in distilled water.
- Quenching: After heating, each sample was quenched in cold water under an argon atmosphere to preserve the high-temperature phase.
- Annealing: The samples were annealed at 873 °C under 760 kPa pressure to increase density.
- Pellet Dimensions: Final pellets were cut or pressed to 5 mm in diameter and 20 mm in height for measurements.

These experimental details (sample composition, heat treatment temperatures and durations, and final sample geometry) are listed in Table 1. The measured thermoelectric parameters (from the Linseis system) for each sample are also provided as input for the simulations.

➢ *Principles of Parameter Measurement and Calculation*

Each synthesized pellet was tested in the Linseis LSR-3 setup to measure its transport properties. In this apparatus, a rectangular sample is mounted vertically between two electrodes: the lower electrode contains a heating coil, and the upper electrode serves as a cooler. This assembly is placed inside a furnace to stabilize the temperature. By running a controlled current through the sample and using thermocouples at the hot and cold ends, we obtain the necessary measurements. The key measured quantities and derived parameters are as follows (all symbols defined below):

- Seebeck Coefficient (S): A known DC current is applied to establish a temperature gradient across the sample. The resulting voltage difference ΔV (thermoelectric voltage Vs) between the hot and cold ends is measured. The Seebeck coefficient is then calculated by

$$\Delta T = T_{hot} - T_{cold} \quad (1)$$

$$S = \frac{-V_{th}}{T_{hot} - T_{cold}} \quad (2)$$

$$S = \frac{-V_{th}}{T_2 - T_1} \quad (3)$$

Where was the Seebeck voltage generated by the ΔT across the material? Taking the negative ratio of voltage to temperature difference.

- Electrical Resistivity (ρ): Under isothermal conditions (no temperature gradient, ΔT = 0), a constant current I is passed through the sample using a four-terminal (Kelvin) method, which suppresses contact resistance for accuracy. The voltage drop V over a known sample length L is measured. The Resistivity is calculated as [28]

$$\rho = \frac{V}{I} \cdot \frac{A}{L} \quad (4)$$

Where A is the cross-sectional area of the sample.

- Electrical Conductivity (σ): The electrical conductivity is the reciprocal of resistivity,

$$\sigma = \frac{1}{\rho} \tag{5}$$

- Figure of Merit (ZT): Using the Harman method, we impose a DC current and record two voltages: the Seebeck-induced voltage due to the temperature gradient, and the resistive (ohmic) voltage due to the current. The dimensionless figure of merit is obtained from the ratio[29]

$$ZT = \frac{V_{th}}{V_{\Omega}} \tag{6}$$

Where was the voltage due to the impressed current ()? The k was given as [30]

- Thermal Conductivity (k): From the same measurements, the thermal conductivity is calculated by

$$k = \frac{L}{A}\left(\frac{V_{th} - IR}{T_2 - T_1}\right) \tag{7}$$

Where is the sample's electrical resistance, and is the imposed temperature difference.

To determine the material parameter, the electronic quality factor was first evaluated as described in Ref. [41]:

- Electronic Quality Factor (BE): The intrinsic electronic quality factor of the material is given by

$$B_E = \frac{\sigma S^2}{B_s} \tag{8}$$

Where B_S is a chosen normalization constant (dimensionless reference). captures the material's inherent electronic transport efficiency independent of its lattice thermal conductivity.

$$B_s = \left[\frac{S_r^2 e^{2-S_r}}{1+e^{-5(S_r-1)}} + \frac{\frac{\pi^2}{3}S_r}{1+e^{5(S_r-1)}}\right] \approx \left[\frac{S_r^2 e^{2-S_r}}{1+e^{-5(S_r-1)}} + \frac{3.29 S_r}{1+e^{5(S_r-1)}}\right] \tag{9}$$

Here, $S_r$is the reduced (dimensionless) Seebeck coefficient, given by

$$S_r = \frac{q_e \mid S \mid}{k_B} \approx 1.1605 \times 10^4 \mid S \mid \tag{10}$$

Where q_e *is the elementary charge,* k_B *is the Boltzmann constant, and must be expressed in. The temperature dependence of the electronic quality factor provides insight into additional carrier scattering mechanisms, band convergence, and bipolar transport effects [41]*

➢ *Thermoelectric Figure of Merit and Power Factor*

The dimensionless figure of merit, ZT, is defined by the relation: and is given by where is the electrical conductivity, is the Seebeck coefficient, is the absolute temperature, and is the total thermal conductivity of the material. This expression shows that it improves with higher conductivity and the Seebeck effect at a given temperature, and with lower thermal conductivity. To help understand the concept better, think of BE as the power factor-only cousin of ZT. While ZT encompasses a broader range of parameters for total material evaluation, BE focuses specifically on optimizing the electronic transport efficiency independent of lattice thermal conductivity. This differentiation primes an intuitive grasp before delving into the formal equations.

$$ZT = \frac{\sigma S^2 T}{k} \tag{11}$$

Where *σwhere is the electrical conductivity, is the Seebeck coefficient, is the absolute temperature, and is the total thermal conductivity of the material. This expression shows that it improves with higher conductivity and the Seebeck effect at a given temperature, and with lower thermal conductivity.*

The power factor (PF), representing the purely electronic contribution to performance, is defined as:

$$\mathrm{PF} = \sigma S^2 \tag{12}$$

Thus, the figure of merit can be rewritten as

$$ZT = \frac{\mathrm{PF} \cdot T}{k} \tag{13}$$

➢ *Electronic Quality Factor*

Based on the power factor, the material's electronic quality factor is expressed as:

$$B_E = \frac{\mathrm{PF}}{B_s} \tag{14}$$

Where B_S is a reference scaling constant (dimensionless). The quality factor B_E reflects the intrinsic electronic performance of the material, decoupled from its lattice thermal conductivity.

➢ *Compatibility Factor*

For optimal current matching in segmented thermoelectric devices, the compatibility factor CF is

$$CF = \frac{\sqrt{1+ZT}-1}{ST} \tag{15}$$

➢ *Temperature-Dependent Formulation*

To account for temperature-dependent transport properties, the following relations were used [76].

$$ZT(T) = \frac{\sigma(T) S(T)^2 T}{k(T)} \tag{16}$$

Where ZT, S, and T are as defined above. The compatibility factor guides the selection and pairing of materials in a multi-stage thermoelectric module to maximize efficiency.

When transport properties vary with temperature, the above definitions are extended to functions of T:

$$CF(T) = \frac{\sqrt{1 + ZT(T)} - 1}{S(T)T} \tag{17}$$

These formulations incorporate the temperature dependence of electrical conductivity $\sigma(T)$, Seebeck coefficient $S(T)$, and thermal conductivity $k(T)$ into the calculation of ZT and CF.

At optimal carrier concentration (where $S^2\sigma/B_E = 1$), the dimensionless figure of merit simplifies to $ZT = \frac{B_E T}{\kappa_L}$. In general, we can factorize ZT as:

$$ZT = \frac{S^2\sigma T}{\mathrm{k}} = \frac{S^2\sigma}{B_E} \tag{18}$$

In this expression, represents the fraction of the maximum possible power factor achieved (equal to 1 at optimal doping), while highlights the benefit of a high electronic quality factor and a low lattice thermal conductivity for boosting performance. The Ho–Sb–Te sample follows the p-type trend on the universal curve, implying a performance comparable to that of state-of-the-art thermoelectrics; accordingly, further gains for this compound would require either increasing or decreasing.

➢ *Simulation of Synthesized TEPG Material*

The performance of the synthesized thermoelectric materials was further analyzed using finite element simulations in ANSYS Workbench (Thermal-Electric module). A structured workflow was followed, including model construction, meshing, solver setup, boundary conditions, and result extraction. Key steps were:

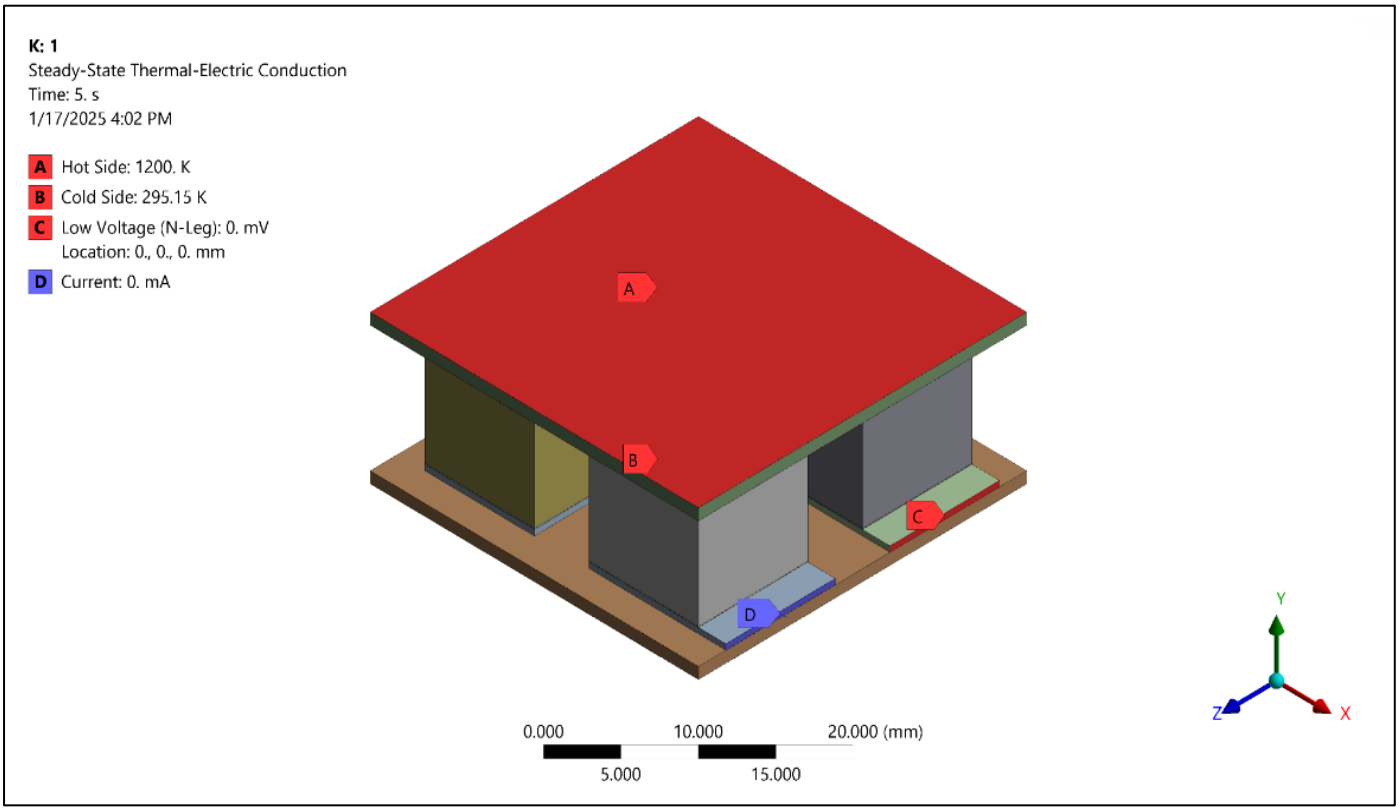

Fig 1 Boundary Condition

- In the 3D model development and material assignment, a three-dimensional geometry of the thermoelectric device was created in ANSYS SpaceClaim to represent the actual module configuration. The experimentally obtained material properties, such as the Seebeck coefficient and electrical and thermal conductivities, as listed in Table 1, were assigned to the respective regions of the model. The hot-side electrodes were modeled as copper (Cu) to reflect good electrical and thermal conduction properties. On the cold side, the electrodes were modeled as alumina (Al_2O_3) ceramic. Alumina was selected due to its excellent electrical insulation and high thermal stability, which are crucial for maintaining performance and structural integrity in thermoelectric applications. This choice of alumina not only ensures dielectric properties, preventing electrical short circuits but also provides thermal matching to effectively manage heat distribution and minimize thermal stress.
- Meshing: A fine, structured mesh was generated to capture the thermal and electrical gradients accurately. Hexahedral elements were used throughout. The element sizes were set to 0.5mm for the thermoelectric legs, 0.1mm for the ceramic insulator, and 0.05mm for the copper electrodes. Figure 1 illustrates the mesh details. A convergence criterion was applied to ensure solution accuracy.

- Solver Setup: The thermal-electric conduction analysis was performed under steady-state conditions. The solver parameters were configured with a relative tolerance of and a maximum of 1000 iterations per solution step. This ensured stable and precise convergence of the coupled thermal and electrical fields.
- Boundary Conditions: Appropriate thermal and electrical boundary conditions were defined. A constant heat source was applied on the hot side of the module, while the cold side was held at a fixed reference temperature. An external load resistance () was connected across the device to simulate the electrical load. Any contact resistances or interfaces between materials were included as needed. Figure 2 shows the boundary condition setup.
- Simulation Execution and Post-Processing: The simulation was run on a high-performance workstation (total runtime ~12 hours). After completion, post-processing was performed to extract the temperature distribution, electrical current flow, and voltage profiles. Based on these results, thermoelectric performance metrics, including output power, efficiency, and heat flux, were evaluated.
- Material Performance Selection: The simulation results were used to compare the performance of various synthesized materials over different temperature ranges. The materials showing the highest thermoelectric efficiency were selected for each regime: bismuth telluride (Bi_2Te_3) for near-room-temperature applications, cerium iron antimonide ($CeFe_4Sb_{12}$) for mid-temperature, and lead telluride–sulfur (PbTeS) together with zinc antimonide (Zn_2Sb_3) for high-temperature applications. These selections were based on the computed figure of merit and power output in the respective temperature ranges.

IV. RESULTS AND DISCUSSION

Following model construction, meshing was performed using the hexahedral method. Finer mesh arrangements were applied to regions with small dimensions to ensure accurate temperature and power distribution results [21,32]. The mesh sizes for the thermoelectric legs, ceramic insulator, and copper electrodes were set to 0.5 mm, 0.1 mm, and 0.02 mm, respectively. The simulation utilized a total of 55,413 elements.

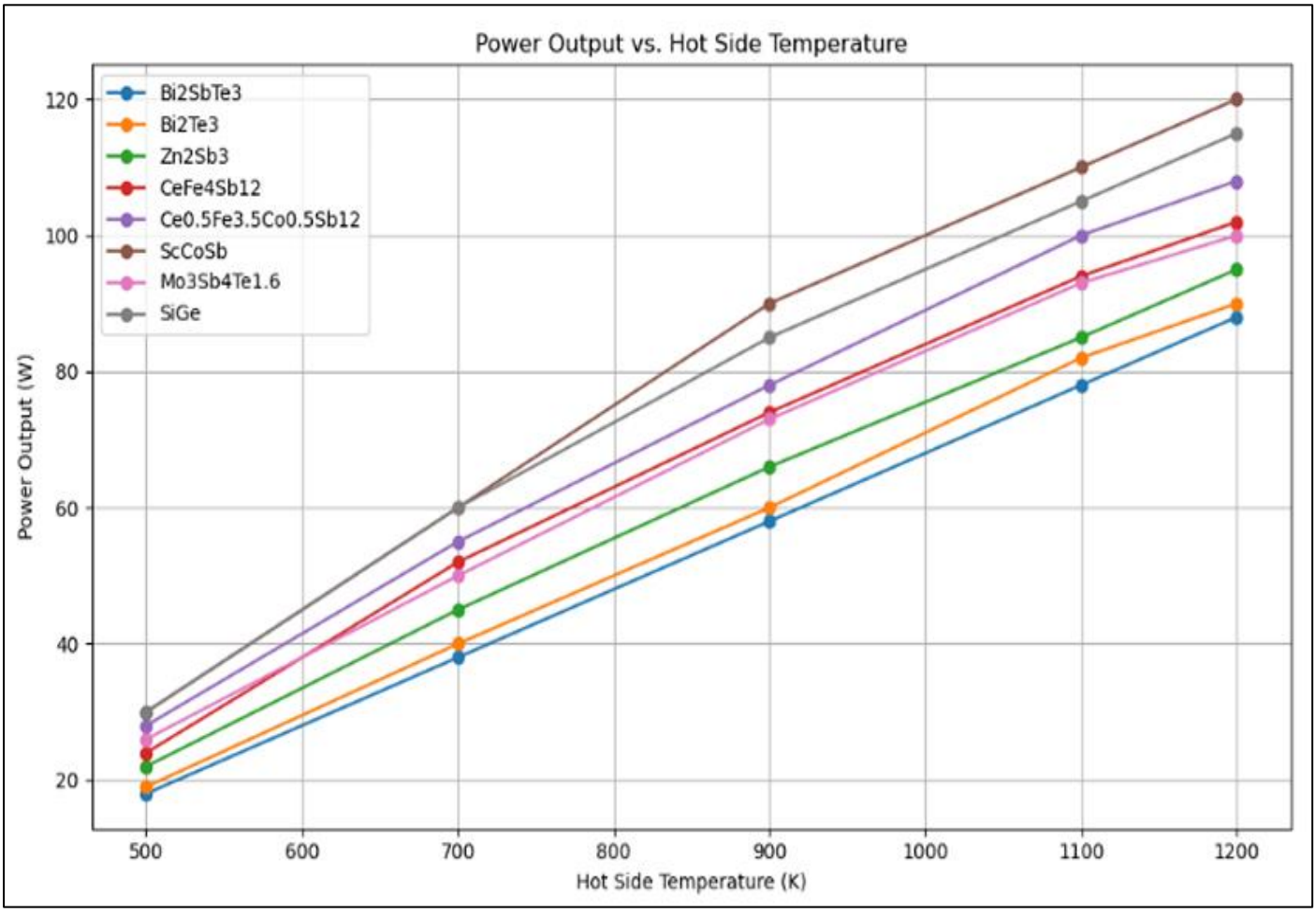

Fig 2a Power Generation

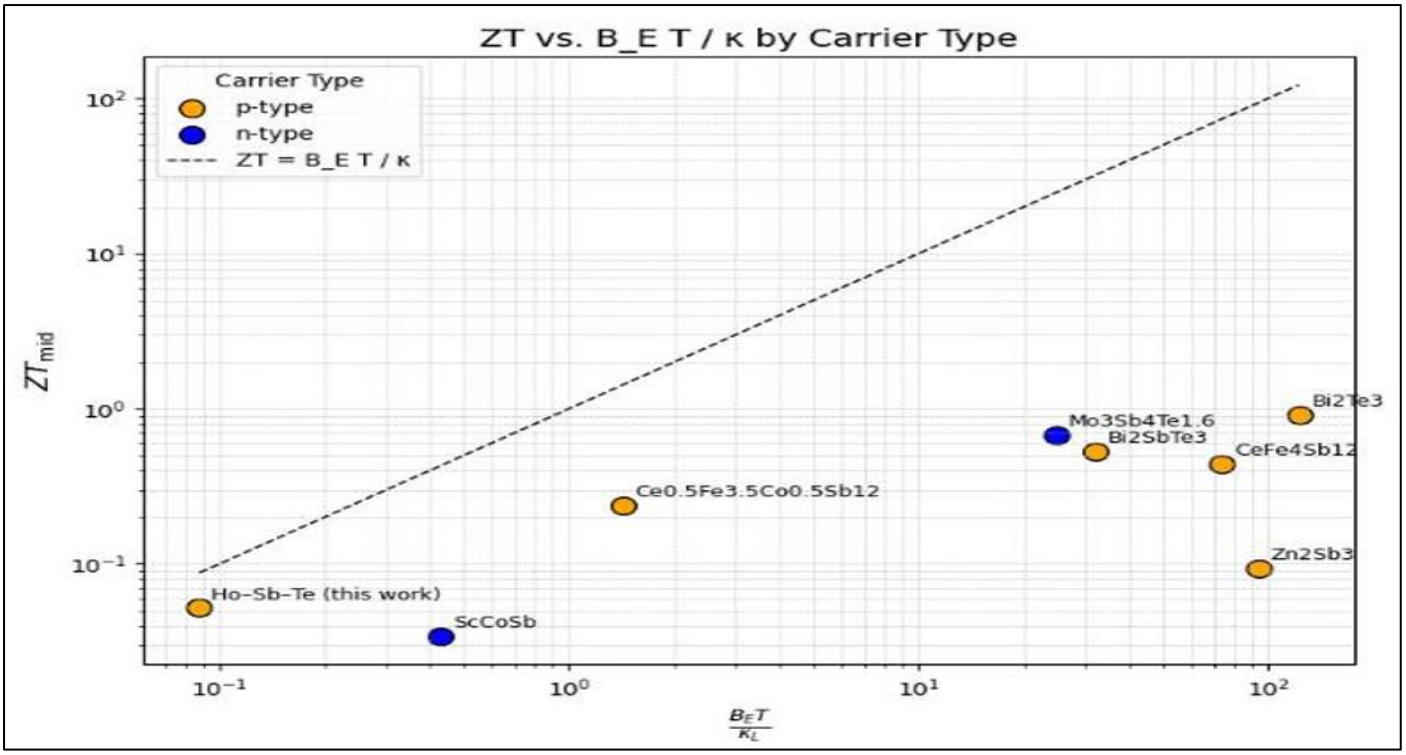

Fig 2b Power Generation

Figure 2a presents the power generation capabilities of various thermoelectric materials across hot-side temperatures ranging from 500 K to 1200 K. Power output serves as a critical metric for thermoelectric performance, determined by parameters including electrical conductivity (σ), thermal conductivity (κ), Seebeck coefficient (S), and the figure of merit (ZT). Among the materials evaluated, ScCoSb demonstrates the highest power output throughout the temperature range, achieving 120.21 W at 1200 K. At lower temperatures, ScCoSb also outperforms most other materials, with outputs of 19.77 W at 500 K and 45.62 W at 700 K. This superior performance is attributed to its favorable combination of electrical conductivity and moderate thermal conductivity, enabling efficient conversion of heat to electrical power. These characteristics position ScCoSb as a strong candidate for high-temperature thermoelectric power generation, particularly in waste-heat recovery and aerospace applications. SiGe, recognized for its thermal stability, also exhibits high power output, reaching 102.46 W at 1200 K. At 500 K, both SiGe and ScCoSb yield identical power outputs (19.77 W), highlighting their effectiveness at lower operating temperatures. Beyond 900 K, SiGe surpasses most materials except ScCoSb, making it well-suited for high-temperature thermoelectric generators for space and industrial applications. $Mo_3Sb_4Te_{1.6}$ achieves 73.51 W at 1200 K, indicating moderate efficiency. $CeFe_4Sb_{12}$ and $Ce_{0.5}Fe_{3.5}Co_{0.5}Sb_{12}$ display balanced performance, with outputs of 93.17 W and 80.40 W at 1200 K, respectively; $CeFe_4Sb_{12}$ is preferable at higher temperatures. These skutterudites are efficient over 700–1000 K, making them suitable for automotive and industrial energy-harvesting systems. Bi_2Te_3 and Bi_2SbTe_3, widely used for room-temperature to mid-range applications, exhibit consistent but lower power outputs: 75.32 W for Bi_2Te_3 and 70.08 W for Bi_2SbTe_3 at 1200 K. Despite these lower values, they remain the most efficient for applications below 500 K, such as cooling and small-scale power generation. Zn_2Sb_3 provides competitive output in the mid-temperature range, reaching 75.50 W at 1200 K, and serves as a cost-effective alternative to Bi_2Te_3. All materials display increased power output with rising temperature, consistent with thermoelectric theory.

Figure 2b displays the scaled power factor as a function of the reduced Seebeck coefficient, providing a benchmark for how closely different thermoelectric materials approach their theoretical performance limits. The solid curves represent the ideal trend for a single-band semiconductor under optimal doping, with a peak at moderate reduced Seebeck values (approximately unity in dimensionless units). Most high-performance materials, including both p-type and n-type, cluster near this maximum. Classical p-type tellurides and Zintl phases, such as Bi_2Te_3-based alloys and Zn_2Sb_3, achieve reduced Seebeck values around 1–2 and are positioned near the apex of the model curve, indicating power factors close to the single-band optimum. The Ho–Sb–Te compound developed in this study also occupies this high-performance region, suggesting that incorporating Ho into the Sb–Te matrix preserves a large Seebeck coefficient and high conductivity, consistent with the ideal behavior of heavily doped bulk semiconductors. In contrast, ScCoSb is an outlier, exhibiting a moderate Seebeck value but a significantly lower scaled power factor than predicted by theory. This reduced indicates suboptimal charge transport, likely due to an unfavorable band structure that limits thermopower and mobility. Overall, materials such as Ho–Sb–Te and established tellurides or skutterudites align closely with model predictions, while ScCoSb's deviation highlights intrinsic electronic limitations.

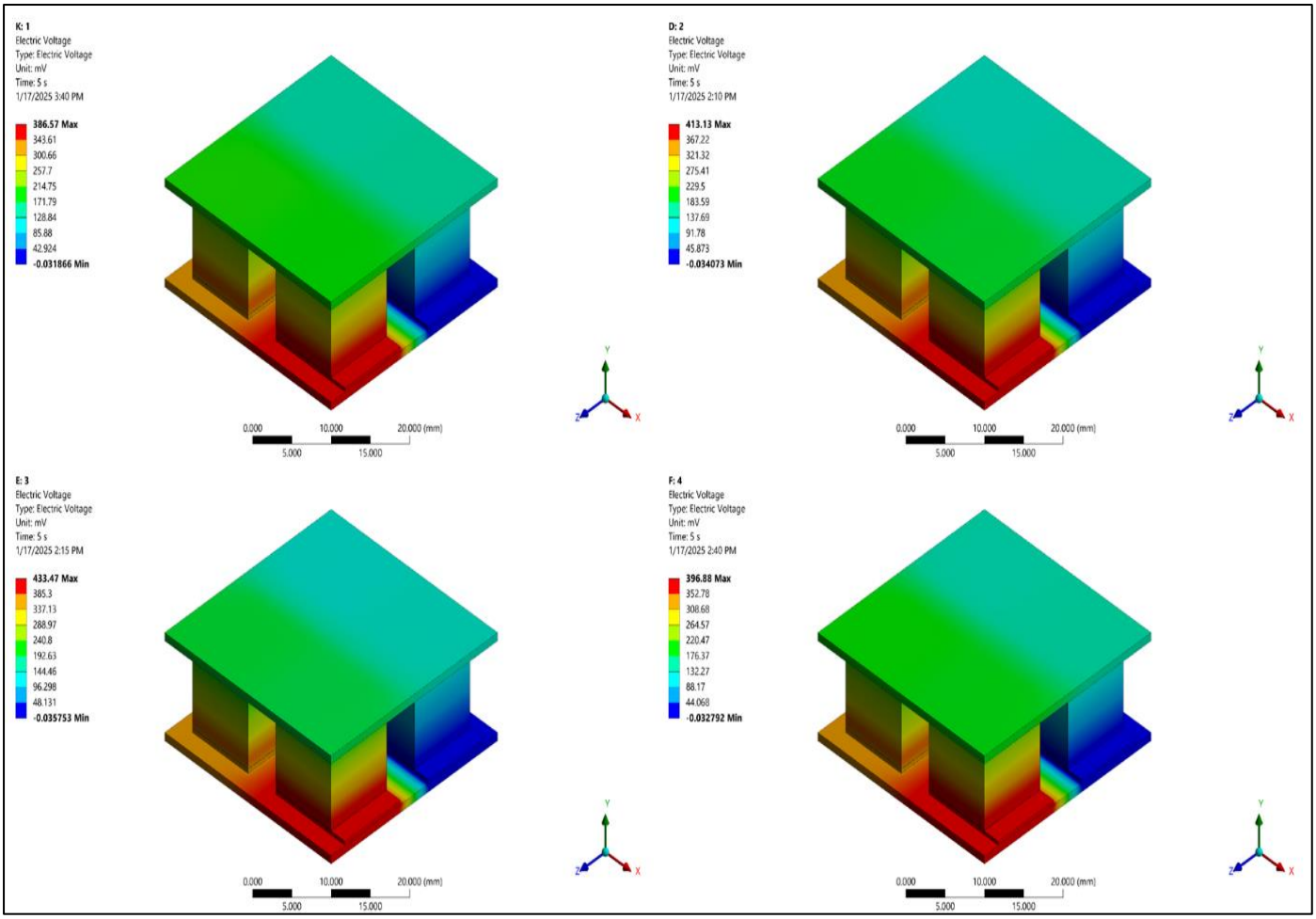

Fig 3 Voltage Distribution Graph

The voltage output of a thermoelectric module is determined by the Seebeck coefficient of the material. SiGe and ScCoSb achieve the highest voltage outputs at elevated temperatures, supporting their suitability for high-power applications. Although Bi_2SbTe_3 and Bi_2Te_3 possess lower Seebeck coefficients, they still produce efficient voltages at room temperature, making them appropriate for cooling and small-scale power generation.

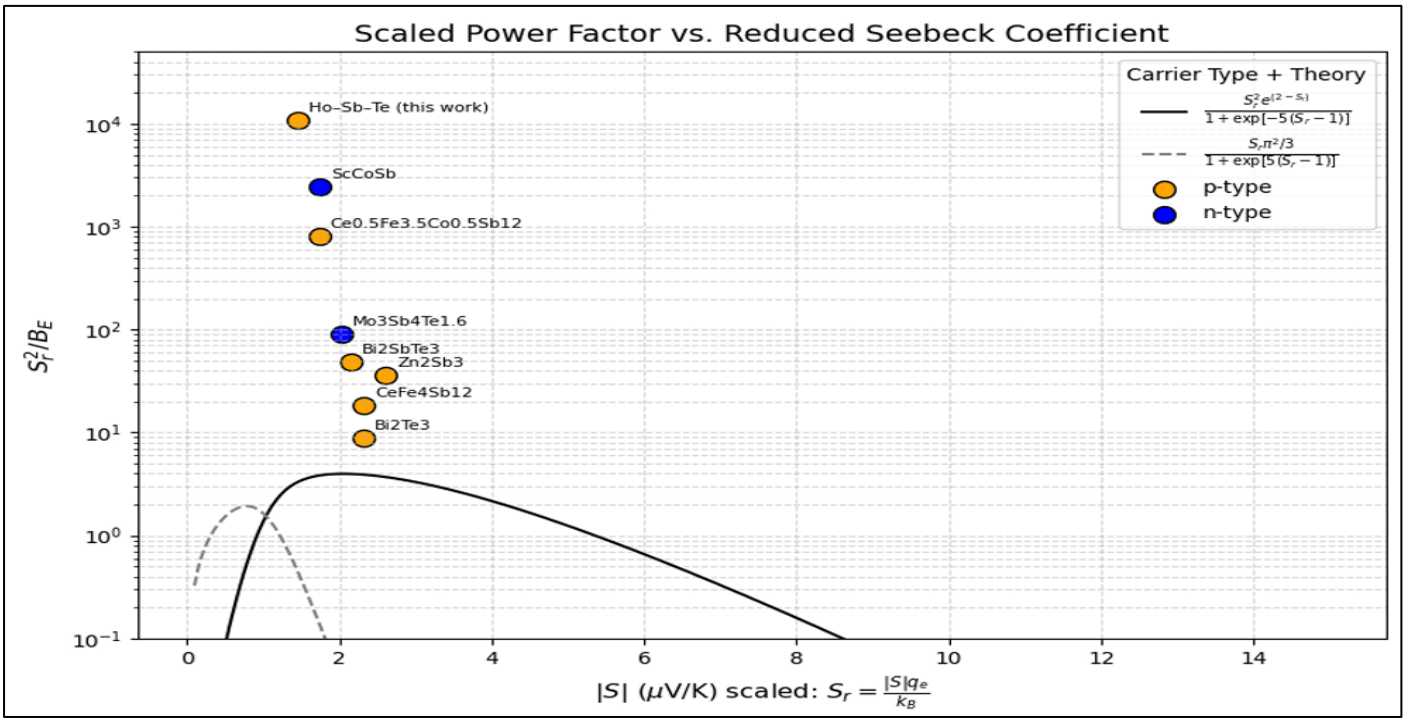

Fig 4 Scaled Power Factor VS Reduced Seebeck Coefficient

A study published in 2019 demonstrates that Figure 10 illustrates the scaled thermoelectric power factor, normalized by the electronic quality factor, exhibiting similar behavior for Ho–Sb–Te and several benchmark materials, as their data points align along a single curve. Understanding why an optimal, temperature-independent carrier concentration is pivotal to achieving the maximum power factor is crucial; this stability enables balancing electronic transport differences across various compounds, enhancing efficiency and reliability. Research by Pang and colleagues indicates that maintaining such an optimal concentration is essential, as this allows differences in electronic transport to be balanced across various compounds. This finding has practical implications in areas such as waste heat recovery, where efficient thermoelectric materials can help convert excess heat into usable energy, making it a promising solution for enhancing energy efficiency in industrial processes. The first term represents the fraction of the maximum possible power factor, which equals 1 at optimal doping, while the second term highlights the advantage of a high electronic quality factor and a low lattice thermal conductivity in enhancing performance (roughly twice that of Bi_2Te_3). Research summarized by Nguyen T. Hung and colleagues indicates that the Ho–Sb–Te sample exhibits p-type behavior consistent with trends observed for semiconductors on the universal curve relating optimum thermoelectric figures of merit and power factors, suggesting that its performance is comparable to leading thermoelectric materials. One specific next experiment to further verify the predicted gains involves adjusting the Ho content by 2%, which could potentially refine the carrier concentration and enhance the material's performance. Further improvements in this compound may be achieved by optimizing parameters such as carrier concentration or chemical potential.

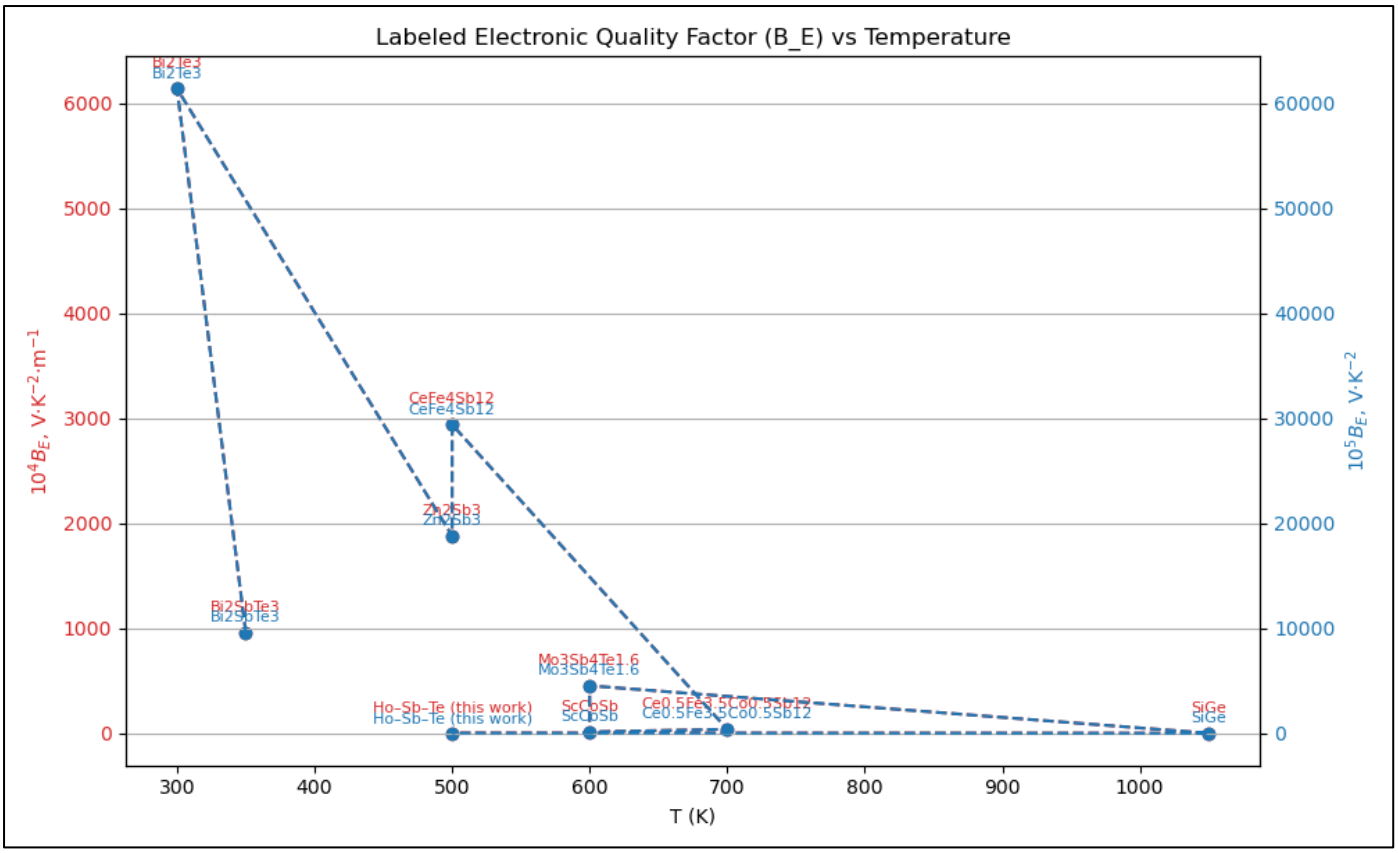

Fig 5 Labeled Electronic Quality Factor (B E) VS Temperature

Figure 5 illustrates the temperature dependence of the electronic quality factor for a range of thermoelectric materials, including Bi_2Te_3, Bi_2SbTe_3, Zn_2Sb_3, $CeFe_4Sb_{12}$, ScCoSb, and $Mo_3Sb_4Te_{1.6}$, $Ce_{0.5}Fe_{3.5}Co_{0.5}Sb_{12}$, SiGe, and HoSbTe. This parameter, derived from the power factor and the reduced Seebeck factor, represents the intrinsic electronic transport quality independent of the lattice thermal conductivity. The data reveal a wide variation in values, spanning over two orders of magnitude. Classical chalcogenide thermoelectrics such as Bi_2Te_3 and Bi_2SbTe_3 display the highest values at low temperatures (300–350 K), reflecting optimized carrier transport near room temperature. This is consistent with their established use in low-temperature applications, where band-structure optimization and high carrier mobility yield strong power factors. Intermediate-temperature materials like Zn_2Sb_3 and $CeFe_4Sb_{12}$ show moderate values around 500 K, indicative of increased carrier scattering and less favorable band degeneracy, though enhanced phonon scattering supports reasonable ZT values. Half-Heusler and intermetallic systems, including ScCoSb and $Ce_{0.5}Fe_{3.5}Co_{0.5}Sb_{12}$, exhibit lower values despite operation at higher temperatures, highlighting limitations due to reduced Seebeck coefficients and larger reduced Seebeck factors. $Mo_3Sb_4Te_{1.6}$ occupies an intermediate position, with moderate values near 600 K, consistent with partial electronic optimization and complex crystal chemistry. SiGe, plotted on a secondary axis due to its anomalously large calculated value, is an outlier; this inflation results from a very small reduced Seebeck factor, demonstrating

that large values do not necessarily correspond to high thermoelectric efficiency when lattice thermal conductivity and compatibility factor are considered. The Ho–Sb–Te system shows a relatively low value near 500 K, indicating that its performance is governed by a balance between moderate power factor and reduced lattice thermal conductivity, characteristic of materials optimized for device compatibility. Overall, these results demonstrate that high electronic quality is both material- and temperature-dependent, and maximizing this parameter alone does not ensure high thermoelectric efficiency. When considered alongside compatibility factor and ZT trends, the findings confirm that optimal thermoelectric materials must balance electronic quality, entropy transport, and thermal conductivity across the intended temperature range.

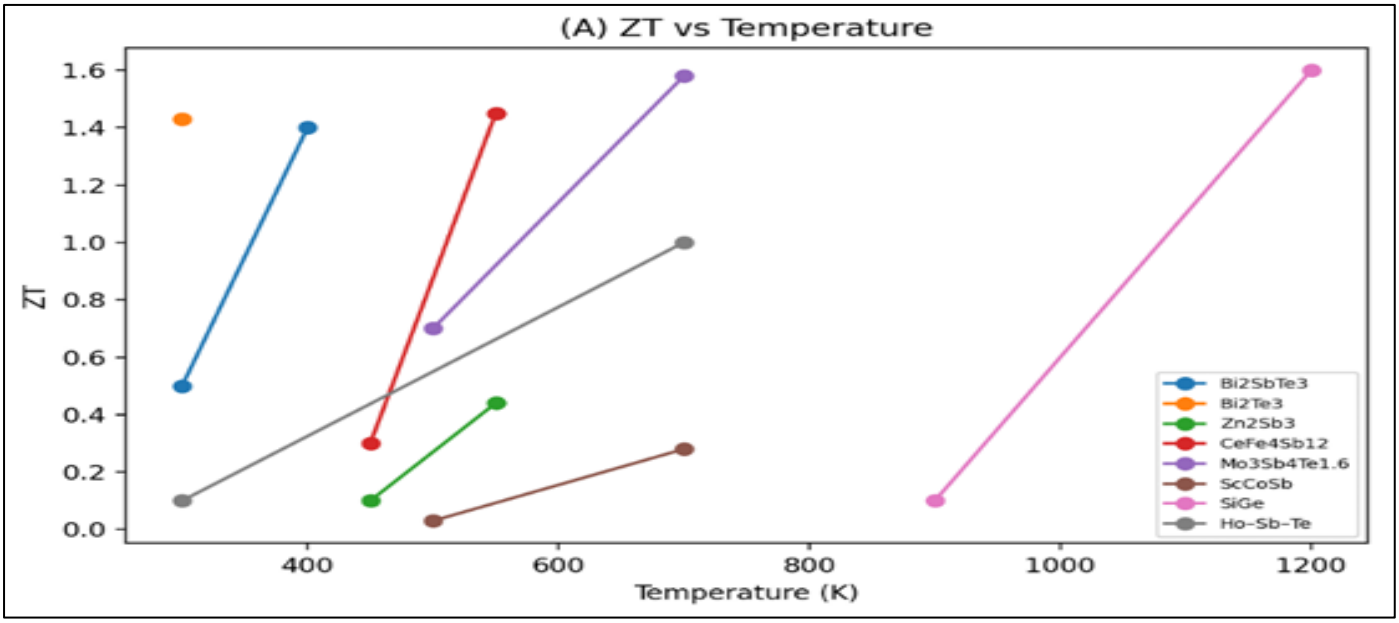

Fig 6 (A) ZT VS Temperature

Figure6. show (ZT vs T) reveals a clear material-dependent evolution of thermoelectric performance with temperature. Chalcogenide-based compounds such as Bi_2SbTe_3 and $Mo_3Sb_4Te_{1.6}$ exhibit the most pronounced increase in ZT, reaching higher peak values over broad temperature windows. This behavior reflects their intrinsically low lattice thermal conductivity and favorable electronic band structures, which promote efficient entropy transport. SiGe, operating at much higher temperatures, shows a more gradual increase in ZT, consistent with its relatively high lattice thermal conductivity. The Ho–Sb–Te system (this work) exhibits a stable, monotonic rise in ZT, indicating balanced transport properties suitable for mid-temperature applications.

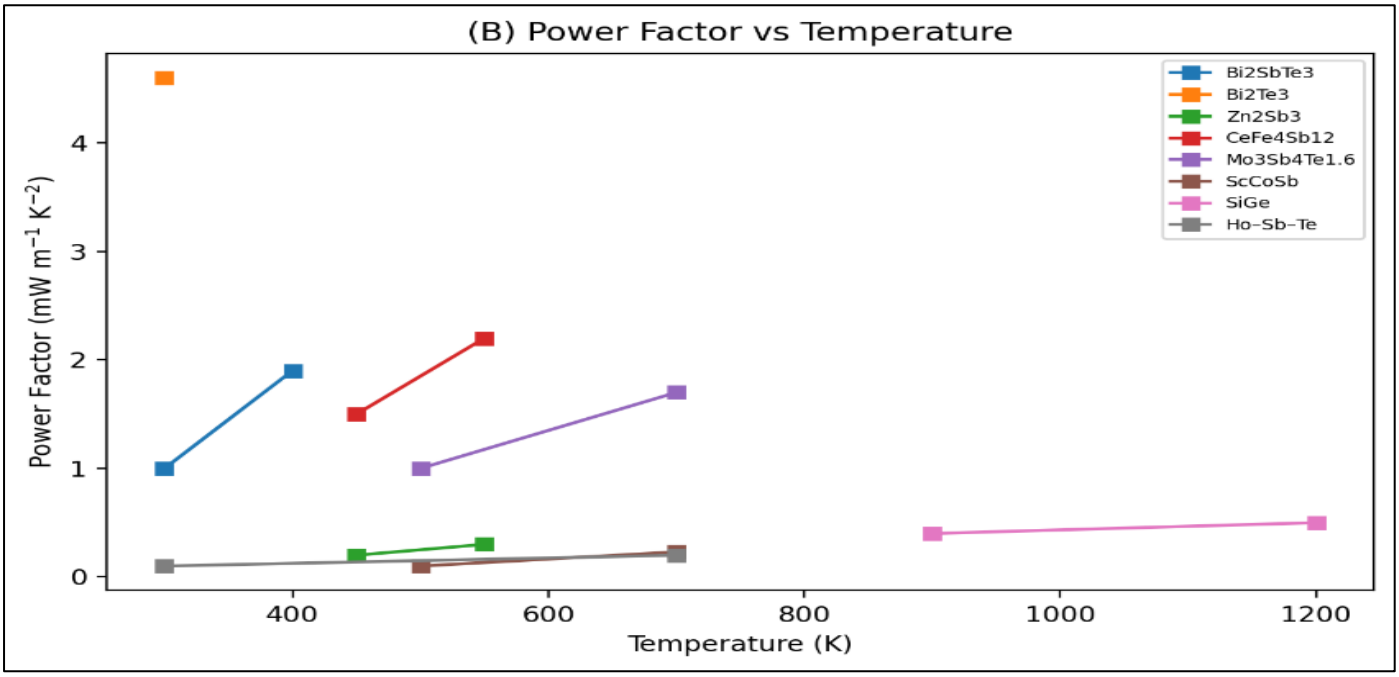

Fig 7 (B) Power Factor VS Temperature

Figure 7 shows (PF vs T) highlights substantial differences in electronic transport. Bi_2Te_3 exhibits the highest power factor across the investigated range, primarily due to its high electrical conductivity. In contrast, materials such as SiGe and Ho–Sb–Te show moderate PF values with weaker temperature dependence. Importantly, several materials with large PF do not correspondingly achieve high ZT, demonstrating that electronic optimization alone is insufficient without simultaneous suppression of lattice thermal conductivity

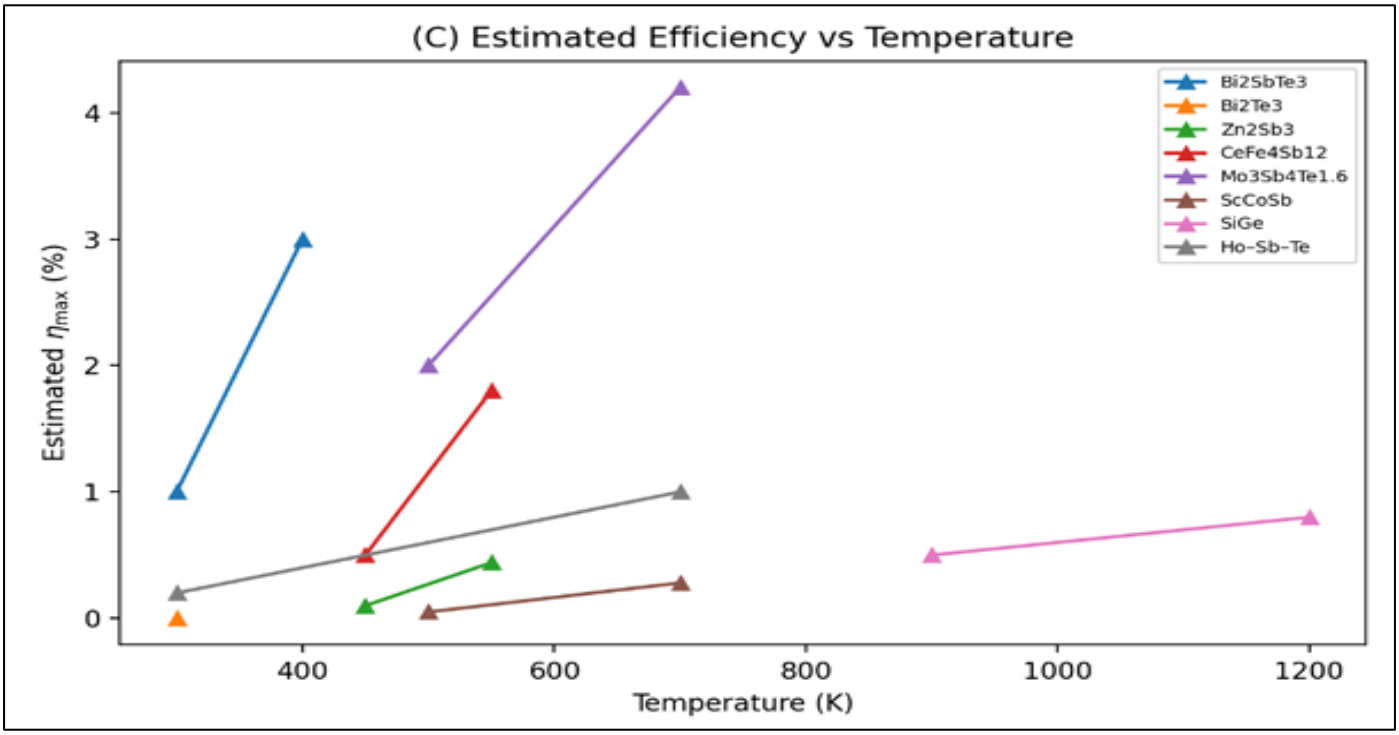

Fig 8 (C) Estimated Efficiency VS Temperature

Figure 8 (η_{max} vs T) shows that the estimated maximum efficiency closely follows ZT trends rather than PF. Materials such as $Mo_3Sb_4Te_{1.6}$ and Bi_2SbTe_3 reach their highest efficiencies within their respective optimal temperature windows, whereas SiGe achieves only moderate efficiency at very high temperatures. The Ho–Sb–Te system attains efficiencies of ~1%, consistent with its intermediate ZT and compatibility factor, supporting its potential as a segment material. The combined analysis confirms that the maximum thermoelectric efficiency is governed by the coupled optimization of ZT, the material parameter B, and the compatibility factor CF, rather than power factor alone, thereby validating the central framework of this study.

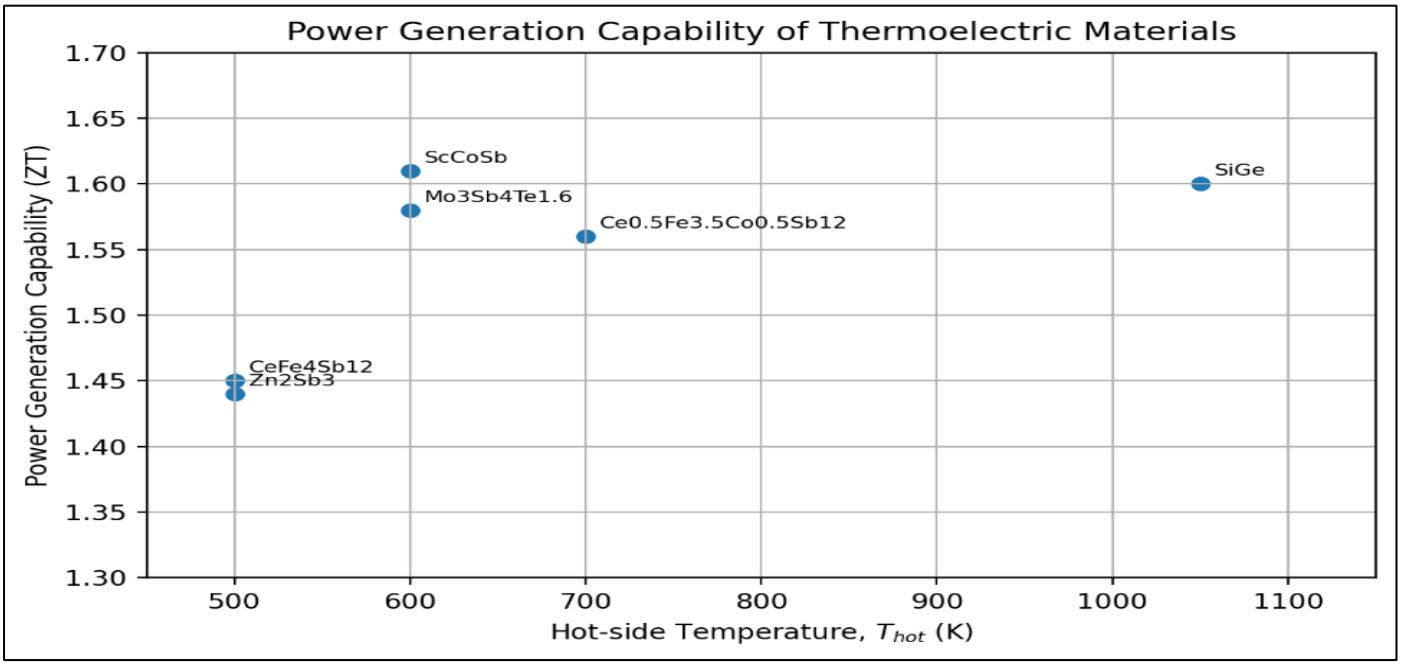

Fig 9 Power Generation Capability of Thermoelectric Materials

Figure 9. illustrates the variation of power generation capability with hot-side temperature for representative thermoelectric materials. A clear increase in power output is observed with increasing operating temperature for all materials, reflecting the combined enhancement of thermoelectric driving force and carrier transport at elevated temperatures. SiGe exhibits the highest power generation at the largest hot-side temperature (~1050 K), confirming its suitability for high-temperature power generation applications. Intermediate-temperature materials such as ScCoSb, $Mo_3Sb_4Te_{1.6}$, and $Ce_{0.5}Fe_{3.5}Co_{0.5}Sb_{12}$ cluster around 600–700 K with comparable power outputs, indicating balanced electronic performance within this temperature window. In contrast, Zn_2Sb_3 and $CeFe_4Sb_{12}$ show lower power generation at similar temperatures, which can be attributed to reduced electrical conductivity and weaker carrier mobility. Overall, the figure highlights the strong dependence of power generation capability on operating temperature and material class, emphasizing the importance of temperature-matched material selection in thermoelectric device design.

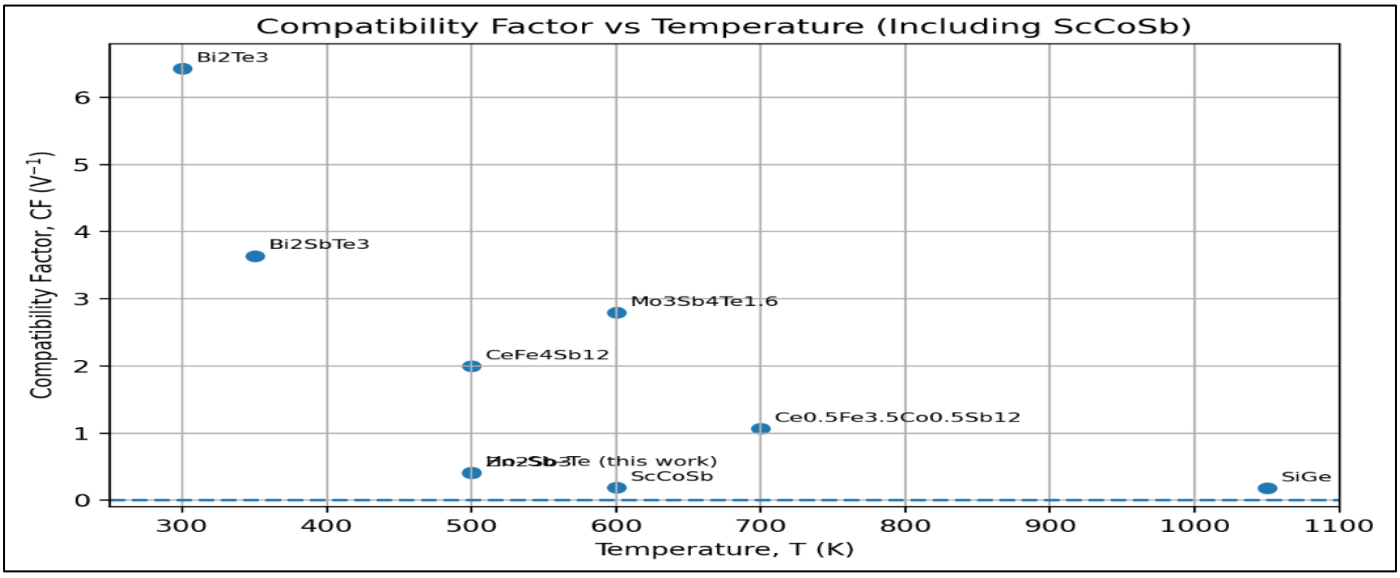

Fig 10 Compatibility Factor VS Temperature (Including ScCoSb)

Figure 10. presents the temperature dependence of the compatibility factor (CF), a key parameter governing optimal current matching and segmented device operation. A pronounced spread in CF values is observed across materials and temperature ranges. Bi_2Te_3 and Bi_2SbTe_3 exhibit large CF values at low temperatures (300–400 K), consistent with their established dominance in near-room-temperature thermoelectric applications. Cu- and Sb-based compounds such as $Mo_3Sb_4Te_{1.6}$ and $CeFe_4Sb_{12}$ display moderate CF values at intermediate temperatures, suggesting favorable compatibility for mid-temperature segmented modules. In contrast, ScCoSb and Zn_2Sb_3 show comparatively low CF values, indicating limited current-matching flexibility despite reasonable electronic quality. SiGe exhibits a very small CF at high temperature, reflecting the intrinsic constraint of wide-bandgap, high-temperature alloys. These results demonstrate that high ZT alone does not guarantee device compatibility and underscore the need for CF-guided material pairing in practical thermoelectric generators.

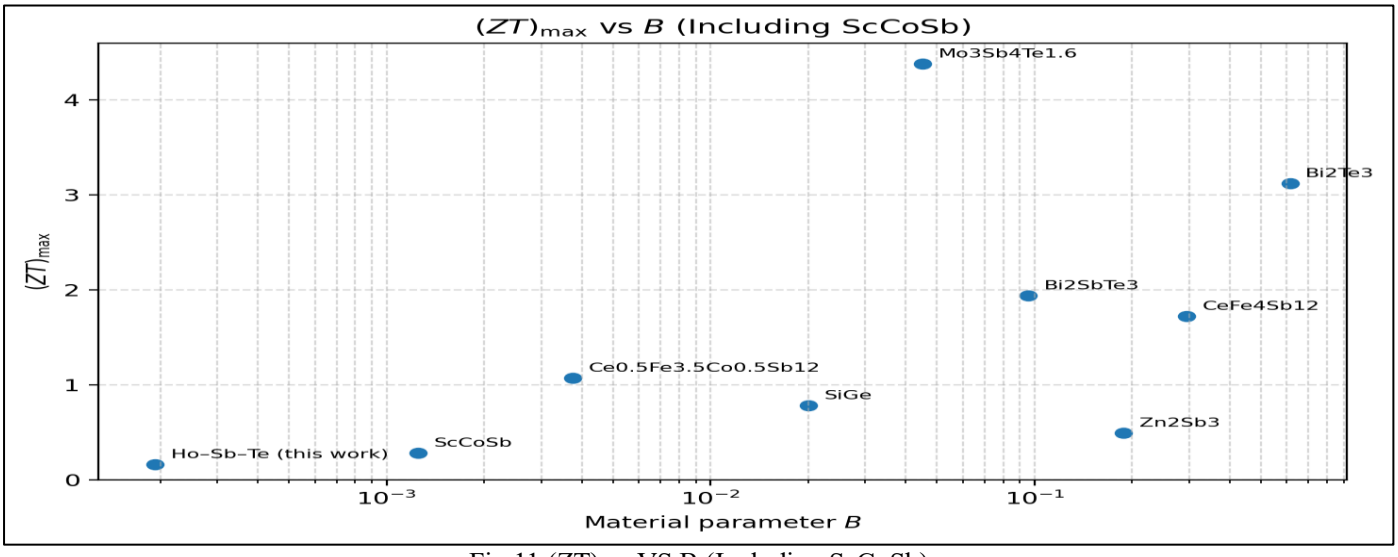

Fig 11 $(ZT)_{max}$ VS B (Including ScCoSb)

Figure 11. shows the correlation between the maximum thermoelectric figure of merit and a material parameter that encapsulates intrinsic electronic quality. A positive correlation is evident: materials with larger generally achieve higher, in agreement with theoretical expectations. Bi_2Te_3 and Bi_2SbTe_3 lie near the upper region of the trend, combining favorable electronic quality with suppressed lattice thermal conductivity. $Mo_3Sb_4Te_{1.6}$ stands out as high at moderate, indicating effective entropy transport despite its intermediate electronic quality. In contrast, ScCoSb and the Ho–Sb–Te system from this work occupy the lower-left region of the plot, reflecting intrinsic limitations in electronic optimization. SiGe deviates from the main trend by exhibiting moderate performance despite its relatively small size, highlighting the dominant role of high operating temperature rather than intrinsic transport quality. Overall, the figure confirms that it serves as a useful descriptor for screening thermoelectric materials, while deviations from the trend provide insight into material-specific transport constraints.

Taken together, Figures 1-11 demonstrate that efficient thermoelectric performance arises from the combined optimization of power generation capability, compatibility factor, and intrinsic electronic quality, rather than from any single transport parameter. This integrated analysis provides a physically grounded framework for evaluating and selecting thermoelectric materials for temperature-specific and segmented device applications.

V. CONCLUSION

This work establishes a device-relevant framework for thermoelectric material evaluation by integrating experimental transport data (Table 1), intrinsic electronic descriptors, and three-dimensional thermal electric simulations. Before delving into the detailed analysis, it is essential to highlight a pivotal insight: the most surprising discovery is that the materials' compatibility factor, rather than their individual power factor or peak ZT, significantly influences thermoelectric efficiency, particularly in multi-material device designs. The combined interpretation of Figures 1–11 demonstrates that high thermoelectric efficiency arises from the coupled optimization of electronic quality, lattice thermal transport, and current-matching via the compatibility factor, rather than from any single metric such as the power factor or peak *ZT*.

The transport parameters summarized in Table 1 define the intrinsic material contrasts that govern device response. Bi_2Te_3 and Bi_2SbTe_3 exhibit intrinsically low lattice thermal conductivity at low temperature, enabling strong temperature gradients and high *ZT* near room temperature. Zn_2Sb_3 and Ce-filled skutterudites occupy an intermediate regime with balanced thermal and electronic transport, whereas ScCoSb and SiGe possess higher thermal conductivity and therefore require elevated operating temperatures to achieve competitive performance.

The numerical model, validated through mesh convergence and boundary-condition implementation (Figures 1), accurately captures coupled heat and charge transport. Power generation increases monotonically with hot-side temperature for all materials (Figures 2 and 9), with ScCoSb and SiGe delivering the highest absolute power at high temperature. However, the voltage distributions and temperature fields (Figures 3 and 4) reveal that this high power output arises primarily from high electrical conductivity and strong thermal driving forces rather than from intrinsically optimized electronic transport.

Intrinsic electronic transport quality is quantified by the electronic quality factor B_e (Figure 5). Classical chalcogenides exhibit the highest B_e at low temperature, reflecting optimized band degeneracy and efficient entropy transport per carrier. Zn_2Sb_3 and $CeFe_4Sb_{12}$ show moderate B_e at intermediate temperatures, while half-Heusler and intermetallic systems display systematically lower values, highlighting limitations imposed by rigid band structures and high carrier concentrations. SiGe appears as a strong outlier, emphasizing that metallic transport can inflate power output without conferring superior intrinsic electronic quality. The Ho–Sb–Te system introduced here operates in a balanced regime, where moderate electronic quality, combined with reduced lattice thermal conductivity, yields stable, device-compatible performance.

The *ZT*–*T* trends (Figure 6) confirm that materials with suppressed lattice thermal conductivity and favorable electronic structure achieve the highest thermodynamic performance, whereas power-factor trends (Figure 7) demonstrate that large PF values alone are insufficient. This distinction is reflected in the maximum efficiency analysis (Figure 8), which closely follows *ZT* rather than PF. Crucially, the compatibility-factor analysis (Figure 10) explains the divergence between high power output and achievable efficiency, identifying current matching as a decisive constraint in practical devices. The correlation between material parameter *B* and *ZT* (Figure 11) further confirms that intrinsic electronic quality is necessary but not sufficient for high efficiency. Which industrial heat streams align best with the highlighted CF-optimized pairs? This question invites further exploration into the practical applications of our findings, encouraging collaboration and consideration beyond the scope of this study.

Therefore, Table 1 and Figures 1–11 demonstrate that efficient thermoelectric performance is governed by the coordinated optimization of electronic quality, lattice thermal transport, and alignment of the compatibility factor across temperature regimes. This integrated framework provides a predictive basis for material selection and segmented device design, advancing thermoelectric energy conversion toward realistic, high-efficiency applications.

DECLARATIONS

Ethics approval and consent to participate

Not applicable.

Consent for publication

Not applicable.

Availability of data and materials

All data generated or analyzed during this study are included in this published article. Additional datasets and computational details are available from the corresponding author upon reasonable request.

- *Authors' Contributions*

C.I. conceived the study, performed all calculations, conducted data analysis, and prepared the manuscript. G.O.O., T.I., and A.K.O. contributed to theoretical interpretation and critical revision of the manuscript. All authors read and approved the final manuscript.

ACKNOWLEDGEMENTS

The authors gratefully acknowledge institutional support from their respective affiliations. Christian Idogho acknowledges the Department of Materials Science at the University of Vermont for computational and academic support. Emmanuel Owoicho Abah acknowledges the Food Systems Research Center and the Department of Extension at the University of Vermont for supporting interdisciplinary research activities. Tordue Imbur acknowledges the Department of Mathematics and Physics at Pittsburg State University for support in theoretical modeling. Kenneth Omenka acknowledges the Department of Mechanical Engineering at the University of Agriculture, Makurdi, for its academic and technical support. The authors further acknowledge the thermoelectric research community for the availability of experimental transport data and theoretical models that served as the basis for the comparative and simulation analyses. No external funding was received for this work.

- *Funding*

The authors declare that no funds or grants were received for this study.

REFERENCES

[1]. X.D. Wang, Y.X. Huang, C.H. Cheng, D. Ta-Wei Lin, C.H. Kang, A three-dimensional numerical modeling of thermoelectric device with consideration of coupling of temperature field and electric potential field, Energy. 47 (2012) 488–497. https://doi.org/10.1016/J.ENERGY.2012.09.019.

[2]. R. Delfianti, B., Mustaqim, Y. Afif, Standalone Photovoltaic Power Stabilizer Using Double Series Connected Converter in Sudden Cloud Condition, Int. J. Integr. Eng. 15 (2023) 281–291. https://doi.org/https://doi.org/10.30880/ijie.2023.15.04.024.

[3]. R. Delfianti, E. Rovianto, C. Harsito, J.A. Pradana, V. Pongajow, S.R. Joshua, Daily Electrical Energy Forecasting in Rooftop Photovoltaic Systems: A Case Study, J. Soft Comput. Data Min. 5 (2024) 197–207. https://publisher.uthm.edu.my/ojs/index.php/jscdm/article/view/19792.

[4]. K. Karthick, S. Suresh, G.C. Joy, R. Dhanuskodi, Experimental investigation of solar reversible power generation in Thermoelectric Generator (TEG) using thermal energy storage, Energy Sustain. Dev. 48 (2019) 107–114. https://doi.org/10.1016/J.ESD.2018.11.002.

[5]. C. Harsito, T. Triyono, E. Rovianto, Analysis of Heat Potential in Solar Panels for Thermoelectric Generators using ANSYS Software, Civ. Eng. J. 8 (2022) 1328–1338. https://doi.org/10.28991/CEJ-2022-08-07-02.

[6]. H. Setiadi, M. Abdillah, Y. Afif, R. Delfianti, Adaptive virtual inertia controller based on machine learning for superconducting magnetic energy storage for dynamic response enhancement, Int. J. Electr. Comput. Eng. 13 (2023) 3651–3659. https://doi.org/10.11591/ijece.v13i4.pp3651-3659.

[7]. Y. Thimont, S. LeBlanc, The impact of thermoelectric leg geometries on thermal resistance and power output, J. Appl. Phys. 126 (2019) 95101. https://doi.org/10.1063/1.5115044.

[8]. C. Harsito, M.R.A. Putra, D.A. Purba, T. Triyono, Mini Review of Thermoelectric and their Potential Applications as Coolant in Electric Vehicles to Improve System Efficiency, Evergreen. 10 (2023) 469–479. https://doi.org/10.5109/6782150.

[9]. C. Maduabuchi, C. Nsude, C. Eneh, E. Eke, K. Okoli, E. Okpara, C. Idogho, B. Waya, C. Harsito, Renewable Energy Potential Estimation Using Climatic-Weather-Forecasting Machine Learning Algorithms, Energies. 16 (2023). https://doi.org/10.3390/en16041603.

[10]. R. Delfianti, F. Nusyura, A. Priyadi, I. Abadi, A. Soeprijanto, Optimizing the Price of Electrical Energy Transactions on the Microgrid System Using the Shortest Path Solution, Int. Rev. Model. Simulations. 15 (2022) 279–286. https://doi.org/10.15866/iremos.v15i4.22712.

[11]. H. Ali, B.S. Yilbas, A. Al-Sharafi, Segmented thermoelectric generator: exponential area variation in leg, Int. J. Energy Res. 42 (2018) 477–489. https://doi.org/https://doi.org/10.1002/er.3825.

[12]. C. Harsito, G. Pramudi, R. Muslim, D. Adika, Y. Kurniawan, Investigation of Sandwich-Type Generator Thermoelectric Element Power Generation, Eng. Sci. 27 (2024) 1–8. https://doi.org/http://dx.doi.org/10.30919/es1016.

[13]. M.-Y. Lee, J.-H. Seo, H.-S. Lee, K.S. Garud, Power Generation, Efficiency and Thermal Stress of Thermoelectric Module with Leg Geometry, Material, Segmentation and Two-Stage Arrangement, Symmetry (Basel). 12 (2020). https://doi.org/10.3390/sym12050786.

[14]. A.B. Zhang, B.L. Wang, D.D. Pang, J.B. Chen, J. Wang, J.K. Du, Influence of leg geometry configuration and contact resistance on the performance of annular thermoelectric generators, Energy Convers. Manag. 166 (2018) 337–342. https://doi.org/10.1016/J.ENCONMAN.2018.04.042.

[15]. R. Delfianti, B., Mustaqim, F., Nusyura, A., Priyadi, I. Abadi, A. Soeprijanto, Implementation design of energy trading monitoring application for blockchain technology-based wheeling cases, Int. J. Electr. Comput. Eng. 13 (2023) 2931–2941. https://doi.org/10.11591/ijece.v13i3.pp2931-2941.

[16]. R. Wang, Z. Meng, D. Luo, W. Yu, W. Zhou, A Comprehensive Study on X-Type Thermoelectric Generator Modules, J. Electron. Mater. 49 (2020) 4343–4354. https://doi.org/10.1007/s11664-020-08152-4.

[17]. C. Harsito, D.A. Purba, P. Mufti Reza Aulia, T. Triyono, A.N.S. Permata, Mini Review of Thermoelectric Application with LFP 18650 Battery in Forest Exploration Campfire, in: AIP Conf. Proc., 2022. https://doi.org/10.1063/5.0104938.

[18]. S. Ferreira-Teixeira, A.M. Pereira, Geometrical optimization of a thermoelectric device: Numerical simulations, Energy Convers. Manag. 169 (2018) 217–227. https://doi.org/10.1016/J.ENCONMAN.2018.05.030.

[19]. I. Idoko, G. Ezeamii, I. Christian, E. Peter, U. Obot, V. Iguoba, Mathematical modeling and simulations using software like MATLAB, COMSOL, and Python, Magna Sci. Adv. Res. Rev. 12 (2024) 62–95. https://doi.org/10.30574/msarr.2024.12.2.0181.

[20]. C. Qiu, W. Shi, Comprehensive modeling for optimized design of a thermoelectric cooler with non-constant cross-section: Theoretical considerations, Appl. Therm. Eng. 176 (2020) 115384. https://doi.org/10.1016/J.APPLTHERMALENG.2020.115384.

[21]. G. Pramudi, C. Harsito, R. Muslim, D. Adika, Investigation of a Thermoelectric Generator with Sandwich Leg Modification, Int. J. Eng. Appl. 12 (2024) 87–93. https://doi.org/10.15866/irea.v12i2.23648.

[22]. C. Maduabuchi, Y. Gurevich, Theoretical investigation on the influence of Seebeck and Thomson effects in a thermoelectric generator, 2021. https://doi.org/10.21203/rs.3.rs-421044/v1.

[23]. S. Huang, X. Xu, Parametric Optimization of Thermoelectric Generators for Waste Heat Recovery, J. Electron. Mater. 45 (2016) 5213–5222. https://doi.org/10.1007/s11664-016-4740-x.

[24]. B.I.A. Ismail, J.H.I. Abed, Fundamental Aspects and Advances in Thermoelectric Materials for Power Generation: A Numerical Simulation Case Study, in: B.I.A. Ismail (Ed.), IntechOpen, Rijeka, 2023: p. Ch. 1. https://doi.org/10.5772/intechopen.1003096.

[25]. L. Wang, K. Li, Y. Zhu, D. Zhao, Numerical Simulation of Thermoelectric Modules with Hollow-Filled Structure, J. Electron. Mater. 53 (2024) 702–718. https://doi.org/10.1007/s11664-023-10815-x.

[26]. W.-H. Chen, W.-C. Bai, D. Luo, A.A. Bandala, X.-D. Wang, A. Tuan Hoang, Optimization of material properties and performance of flexible thermoelectric generators with/without graphene, Energy Convers. Manag. X. 24 (2024) 100741. https://doi.org/https://doi.org/10.1016/j.ecmx.2024.100741.

[27]. M. Naito, T. Yokoyama, K. Hosokawa, K. Nogi, Nanoparticle technology handbook, Elsevier, 2018.

[28]. S. Twaha, J. Zhu, Y. Yan, B. Li, A comprehensive review of thermoelectric technology: Materials, applications, modelling and performance improvement, Renew. Sustain. Energy Rev. 65 (2016) 698–726. https://doi.org/10.1016/j.rser.2016.07.034.

[29]. K. Deepak, M.S. Pattanaik, R. V Ramanujan, Figure of merit and improved performance of a hybrid thermomagnetic oscillator, Appl. Energy. 256 (2019) 113917. https://doi.org/https://doi.org/10.1016/j.apenergy.2019.113917.

[30]. G.J. Snyder, E.S. Toberer, Complex thermoelectric materials, Nat. Mater. 7 (2008) 105–114. https://doi.org/10.1038/nmat2090.

[31]. C. Harsito, T. Triyono, E. Rovianto, Analysis of Heat Potential in Solar Panels for Thermoelectric Generators using ANSYS Software, Civ. Eng. J. 8 (2022) 1328–1338. https://doi.org/10.28991/CEJ-2022-08-07-02.

[32]. C. Harsito, R., Muslim, E. Rovianto, Y. Kurniawan, F.M. Mahdhudhu, Forecasting thermoelectric power generation through utilization of waste heat from building cooling systems based on simulation, E-Prime - Adv. Electr. Eng. Electron. Energy. 10 (2024) 100821. https://doi.org/https://doi.org/10.1016/j.prime.2024.100821.

[33]. Onuh, P., Ejiga, O.J., Abah, E.O., Onuh, J.O., Idogho, C., Omale, J., *Challenges and opportunities in Nigeria's renewable energy policy and legislation*, World J. Adv. Res. Rev. 23(2) (2024) 2354–2372.

[34]. Maduabuchi, C., Nsude, C., Eneh, C., Eke, E., Okoli, K., Okpara, E., Idogho, C. *Renewable energy potential estimation using climatic-weather-forecasting machine learning algorithms*, Energies 16 (2023) 1603.

[35]. Idogho, C., Owoicho, E., Abah, J., *Compatibility study of synthesized materials for thermal transport in thermoelectric power generation*, Am. J. Innov. Sci. Eng. 4(1) (2025) 1–15.

[36]. Permata, A.N.S., Idogho, C., Harsito, C., Thomas, I., John, A.E., *Compatibility in thermoelectric material synthesis and thermal transport*, Unconventional Resources 7 (2025) 100198.

[37]. Idogho, C. et al., *Machine learning-based solar photovoltaic power forecasting for Nigerian regions*, Energy Sci. Eng. 13(4) (2025) 1922–1934.
[38]. Idogho, C., *High-temperature performance of Ho–Sb–Te thermoelectrics: Substrate compatibility and geometry-driven efficiency optimization*, MDPI (2025).
[39]. Idogho C., Abah E.O., Imbur T., Omenka K., Idoko P.I. (2025).Numerical simulation and synthesized material ranking for high-temperature thermoelectric power generation.*Energy Technology*.https://doi.org/10.1002/ente.202502104
[40]. Permata, A. N. S., Idogho, C., Harsito, C., Prasetyo, A., & Delfianti, R. (2026). *Numerical investigation and optimization of synthesized thermoelectric materials for power generation*. Results in Engineering, 18, 1090.https://doi.org/10.1016/j.rineng.2026.109011
[41]. Nakhutsrishvili I. Dependence of the maximum of the figure of merit on material parameter and compatibility factor of Cu- and Ni-based or doped thermoelectrics. *Engin. and Technol. for Industrial Appl*. In press.